Collective Information and Communication in Morphologically Distinct Astrocytes

Authors:

Nicholas J. Mennona[1,2], Barbara Barile[3], Hoony Kang[1,2], Valentina Benfenati[4], Grazia P. Nicchia[3], Kate M. O'Neill [1], Wolfgang Losert [1,2]

1 Institute for Physial Sciences & Technology, Univ. of Maryland, Col. Park, College Park, MD, USA
2 Physics Dept., Univ. of Maryland, Col. Park, College Park, MD, USA
3 Biosciences, Biotechnology and Environment, University of Bari Aldo Moro, 70125, Bari, Italy
4 Institute of Organic Synthesis and Photoreactivity, National Research Council of Italy, 40129, Bologna, Italy

Keywords: Collective Dynamics, Correlation, Information Theory, Morphology

Abstract:

The activity patterns in astrocytes are of considerable importance, given the recent finding that individual astrocytes actively integrate information from neuronal groups. This work analyzes collective information capacity and information flow of *in vitro* astrocyte networks themselves. We investigate group Ca^{2+} dynamics in several astrocyte phenotypes – polygonal, stellate, and reactive – which represent distinct cytoskeletal architectures with differences in cell-cell coupling that may affect information flow within astrocyte networks. All morphologies are present in the brain to varying degrees at different physiological states. To gain insights into the ability of astrocyte networks to respond to changes in the extracellular environment, we probe the networks with perturbations affecting their activity levels (ATP) and their cytoskeletal dynamics (Latrunculin B). Correlation analysis yields a uniform speed of communication, consistent with the speed of Ca^{2+} waves, confirming that Ca^{2+} serves as the primary mode of information exchange independent of morphology and extracellular environment. To obtain a quantitative metric of group communication, we measure the entropy and partitioned (time-dependent) entropy of the Ca^{2+} dynamics. We find that communication metrics vary depending on astrocyte morphological phenotype and environmental perturbations, indicating that astrocytes' roles in communication may shift with development and microenvironment.

Introduction:

Astrocytes are the most numerous glial cell type in the brain. They are important for physiological functions including K^+ clearance[1] , glutamate homeostasis[2] , and extracellular volume regulation[3] (reviewed in[4]). Their direct importance in brain function has been recognized recently, building on the finding that astrocytes form tri-partite synapses by coupling to synapses between neurons, allowing them to directly impact information transfer in the brain[5]. Thus they can contribute to neuronal signal input integration[6] and other cognitive functions. Indeed, the tight coupling of astrocyte excitability and neuronal activity experimentally and theoretically has become increasingly recognized and confirmed[7,8]. By linking to multiple synapses, astrocytes can integrate information and modulate networks[9]. Indeed, although research on gliotransmission has added to the fundamental picture of communication within the

brain, much is still unknown about the methods with which astrocytes decode functional transients,[10] and their role in brain function[11].

Astrocytes also directly interact with other astrocytes, communication that is governed by slow Ca^{2+} waves[12]. Recent work has focused on single cells and shown that these calcium waves are heterogeneous[13] and flow through astrocyte processes and microdomains[14–16]. These morphological features are thought to be important, with morphological plasticity of astrocytes implicated in synaptic remodeling[17]. Moreover, the morphological heterogeneity of astrocytes is thought to be dependent upon neuronal cues[18].

The current study contrasts three physiologically relevant morphologies of astrocytes, focusing on their collective (group) dynamics. The morphologies – polygonal, stellate, and reactive – are broadly classified as healthy, immature, and injured, respectively, and have distinct physiological phenotypes [15,19–21]. Astrocytes are slow communicators and, therefore, it was necessary to modify the methodology that has previously been used to study collective activity of neurons. Thus, with the goal of broadening understanding of astrocyte-specific network signaling, we quantify the collective dynamics (both spontaneous and perturbed) of these morphologically distinct astrocytes, focusing on the information capacity and information flow among the cell group. We also take advantage of the slow dynamics of astrocytes to quantify their speed of information flow. In addition, we analyze the information capacity embedded within individual astrocytes to functionally understand the intrinsic signaling dynamics of astrocytes operating within a network. These quantitative metrics of collective activity allow us to distinguish different physiological states and environment.

Materials/Methods:

Cell Culture

Astrocytes were prepared from 0-to-2 day postnatal (P0-P2) Sprague Dawley rat brains as described previously[22]. Briefly, cortical tissue from each pup was separately dissociated via trituration, filtered, and plated into T25 flasks containing DMEM (ThermoFisher), 15% fetal bovine serum (Benchmark), and 1% pencillin-streptomycin (P/S). After roughly 7 days, in order to generate stellate and reactive astrocytes, the media was changed to either (1) stellate media, which includes Neurobasal (ThermoFisher), 2% B27+ (GIBCO), 5 ng/mL HB-EGF (TOCRIS BioSciences)[15] or (2) reactive media, which is serum-free DMEM to which 10 ug/mL of TGF-B1 was added after 5 additional days *in vitro*[23].

Imaging

Experiments were performed between 14 to 21 days after dissection[24]. At this time, astrocytes were trypsinized from flasks and plated into PDL-coated (Sigma-Aldrich) 35 mm dishes (MatTek). Dishes containing cultured astrocytes were incubated with 5μM CalBryte 590 AM (AAT Bioquest) for 30-60 min at 37°C prior to imaging. Dishes were then washed with PBS. Astrocytes are plated at densities such that they proliferate to roughly 500k cells/well on the day of imaging (a final density of approximately 10k cells/mm^2), and imaging was performed on a spinning disk confocal microscope (PerkinElmer). Image acquisition occurred for approximately 15 minutes at roughly 1 frame per second with 100 ms of exposure time per frame.

All experiments are performed in NeuroBasal media (Gibco). We use this media to simulate a neuronal environment, and we found that it induces activity in unperturbed wells. ATP (Sigma-Aldrich) and Latrunculin B (Sigma-Aldrich) were applied immediately upon imaging and at low-dose concentrations of 1.5uM for ATP and 0.5uM for Latrunculin B. Unlike Latrunculin A, the slower depolymerization rate of Latrunculin B allows for perturbation of actin without drastically dissociating the entire astrocyte network. Therefore, once optimization was complete, we only used Latrunculin B for our experiments.

Cell lysis and Western Blot:

Protein samples were obtained as previously described with some slight changes[3]. Briefly, astrocytes grown for 7 days in control, stellate and reactive media were washed in ice-cold phosphate-buffered saline (PBS) and scraped with 300 µL of RIPA lysis buffer (10 mM Tris-HCl, pH 7.4, 140 mM NaCl, 1% Triton X-100, 1% Na deoxycholate, 0.1% SDS, 1mM Na3VO4, 1 mM NaF, 1 mM EDTA and 1× Protease Inhibitor Cocktail). Lysates were vortexed every 5 minutes for 30 minutes and centrifuged at 22 000 for 30 minutes at 4°C. Supernatants were collected and Pierce™ BCA Protein Assay Kit was used to dose the protein content. 5 µg of proteins/lane were dissolved in Laemmli Sample Buffer (Bio-Rad, Hercules, California, USA) added with 50 mM dithiothreitol, heated to 37°C for 10 min and resolved by SDS-PAGE in 10% (for Cx43 detection) and 12% (for AQP4 and GFAP detection) gels prepared with Mini-PROTEAN TGX Stain-Free Precast polyacrylamide solutions (Bio-Rad, Hercules, California, USA). gels were then activated for 5 minutes on a Chemidoc imaging system (Bio-Rad, Hercules, California, USA) and transferred to polyvinylidene fluoride (PVDF) membranes (Merck Millipore, Burlington, Massachusetts, USA). Stain-free signal of transferred blots was collected. Membranes were incubated with blocking solution and incubated overnight with primary antibodies, rinsed, then incubated with the appropriate peroxidase-conjugated IgG secondary antibodies. Protein-specific bands were revealed using enhanced chemiluminescent Clarity Western ECL Substrate (Bio-Rad, Hercules, California, USA) and visualized on a Chemidoc imaging system. The densitometric analysis was performed in Image Lab software 6.1.0 by normalizing the bands to the stain-free blot signal. The Western blot analysis of Cx43, AQP4, and GFAP for the polygonal, stellate, and reactive astrocytes confirms three distinct phenotypes; reactive upregulate Cx43 and AQP4, stellate upregulate AQP4, and polygonal cells do not express any of these markers significantly.

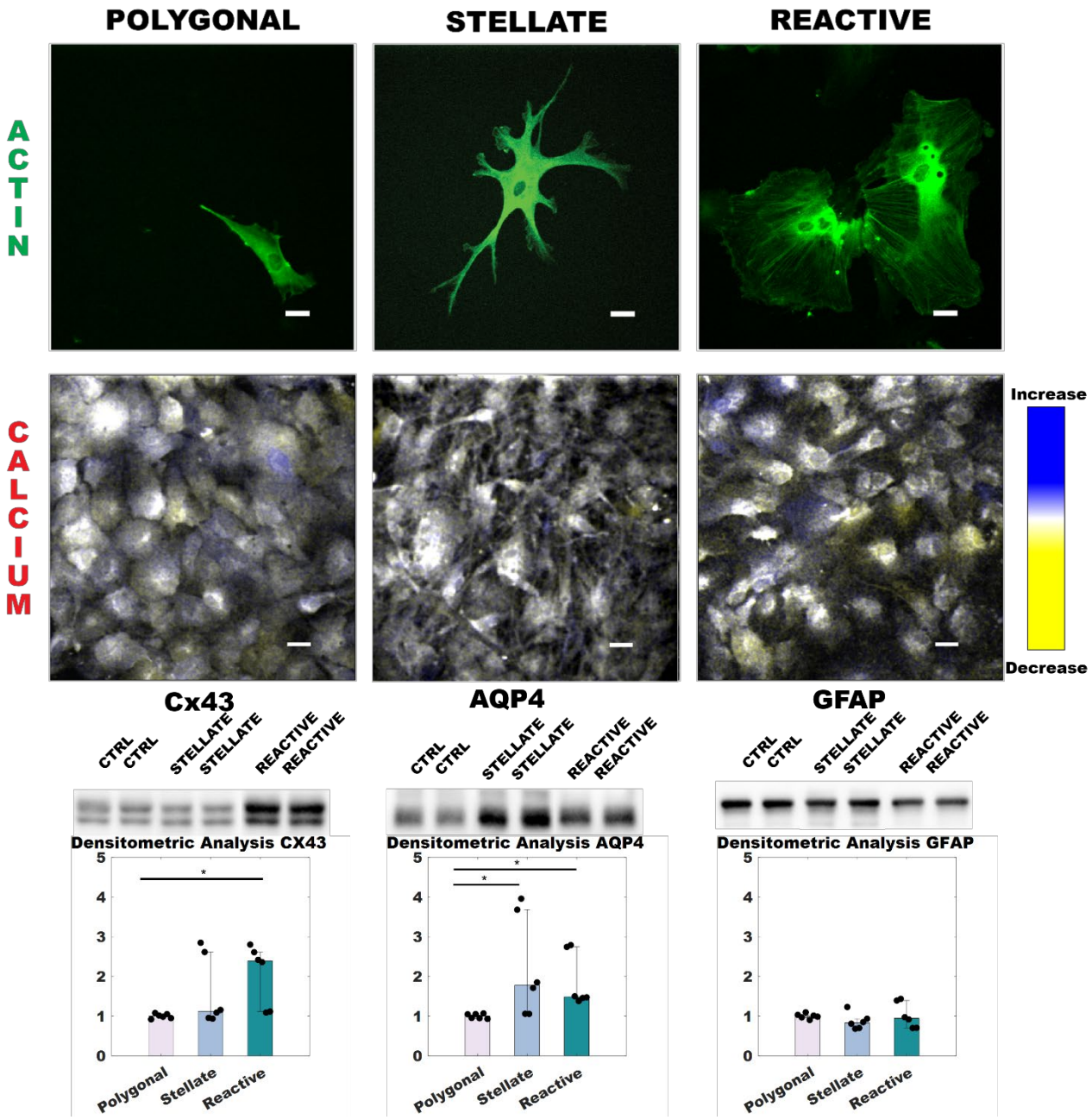

*Fig 1: Astrocyte morphologies (polygonal, stellate, and reactive). The phenotypes correspond to different morphologies as shown in green via actin images. Images of actin are acquired with 488nm light of astrocytes that express BacMam Actin-GFP. We record the calcium signaling channels of these dense astrocyte networks with 561 nm light of astrocyte networks stained with Calbryte 590. It has been noted that, regardless of protocol, different media formulations result in different morphologies for astrocytes[15]. We use time-overlays to show the different manifestations of calcium propagation in the distinct morphological conditions of astrocytes. Blue corresponds to an increase in [Ca^{2+}] during this frame, yellow a decrease, and white means that this frame contains values similar to the previous timepoint. Westerm Blot analysis of Cx43, AQP4, and GFAP in polygonal, stellate, and reactive astrocytes. The upper panels show Cx43 (band at ~43kDa), AQP4 (band at ~30-32 kDa), and GFAP expression (band at ~50 kDa) in primary rat astrocytes. Western Blot analysis of Cx43, AQP4, and GFAP in polygonal, reactive and stellate astrocytes. A. Upper panels: Western Blot showing Cx43 (band at ~43 kDa), AQP4 (band at ~30-32 kDa), and GFAP expression (band at ~50 kDa) in rat astrocytes. Using a Kruskal Wallis Dunn's multiple comparison test, we find significant compared to polygonal for stellate (AQP4) and reactive (Cx43 and AQP4). *$p< 0.05$; **$p<0.01$. Scale bars are 25 µm.*

Results

Spatial and Temporal Relationships in Astrocyte Networks

In this work we investigate astrocytes of three morphological types. Fig. 1 (top) provides representative images of the three classes of astrocytes analyzed in this study. For these astrocyte types we investigate collective Ca^{2+} dynamics as illustrated in Fig 1 (middle). Biologically, we find that the three phenotypes have distinct gene expressions of key proteins related cell-cell communication (Gap junction protein CX43, water channel aquaporin 4) as shown in Fig 1 (bottom).

To analyze the calcium dynamics of astrocytes, we first segment individual astrocyte objects within our imaging datasets using the morphological watershed algorithm, FogBank[25]. We manually refined parameters per each imaging sequence such that segmented boundaries roughly correspond to the distinctions made by eye, as seen Fig. 2A. FogBank preserves the unique heterogeneity of astrocyte bodies rather than using the cell center with an arbitrary radius, as is typically done with neuron-imaging analysis[26]. All image sequences are jitter corrected and Gaussian smoothed in the spatial domain before further analysis. For each frame in a dataset, we take the median fluorescence value from all the pixels identified within the astrocyte object as shown in by the five objects in Fig 2B. We compute relative fluorescence measure ($\Delta F/F_0$), where $\Delta F=F-F_0$, for each astrocyte object. F_0 is computed using a window of approximately 30-s (30 frames, 15 back, 15 forward) where F_0 is the average of the fluorescence values below the 50th percentile of values contained within the window[27]. We chose this window size based upon experimental observation of astrocyte calcium event duration. Traces are then smoothed. These calculations ($\Delta F/F_0$) are performed in MATLAB. Examples of such traces are shown in Fig 2C.

An additional filtering step is applied before further analysis. Our goal is to use traces that show persistent (coarsely 'active') behavior in the networks. Persistence indicates high autocorrelation. Contrariwise, anti-persistence means the opposite: each time step in a time series wildly fluctuates. For any arbitrary astrocyte spike, we know it should have a significant time duration to its event. Therefore, the positive (calcium ramp) should persist for some number of frames followed reliably by a decline for some number of frame. On the other hand, white noise is anti-persistent since, for any given timestep, there exists a 50% chance for increasing or decreasing behavior. We want to filter these traces out as such data represent either poor segmentation or mean background noise fluctuations. Moreover, an astrocyte that flickers once during an imaging sequence does not qualify. Similarly, low-level fluctuations above noise but below a meaningful behavior pattern should be filtered out, so we use the Hurst exponent as a metric for this filtering. The Hurst exponent is a measure that more rigorously quantifies the autocorrelation of any given time series[28]. It also provides a reliable and standardized method for removing traces that are classifiable as noise or relatively inactive astrocytes. Based upon observation of inactive and active cells and networks, we filter out traces with a Hurst exponent below 0.4, which worked well for our data. As some traces that passed through the filter still quantify as noise due to their stable fluctuations, we apply an amplitude filter to remove traces that exhibit low-level fluctuations. From the original number of traces provided, compared to the ones not filtered out by the Hurst exponent, we can derive a metric of 'active percentage' in our imaging sequences. The Hurst code was taken from MATLAB's file exchange[29].

To address population-level information processing in astrocyte-specific networks, we apply cross correlation to the traces identified using FogBank and DF/F. The importance of correlations in neuronal encoding is well-cited in the literature[30–33].The study of correlation in the brain relates to the collective activity of neuronal ensembles in relation to information encoding

and processing in the brain. This level of mathematical rigor has not been applied to astrocyte-only networks, and the study of correlation within astrocyte networks has only been viewed in the context of neuronal activation[34]. Thus, we chose to address astrocyte-specific networks in a manner comparable to neuronal network analysis. Physically, at any given time point, Pearson correlation can be used to understand the simultaneity of events from separate traces, see the temporal window in Fig 2D. However, due to the slow, oscillating calcium waves present in astrocyte networks, cross correlation allows us to assess the spatial propagation of calcium information, as shown by the shifted traces in Fig 2G. A visualization of the differences between these two metrics (Pearson and cross correlation) is shown in Figs. 2E,H, respectively. Due to the slow dynamics of astrocytes (i.e. their firings are not as simultaneous nor as quick as neuronal firing), we leverage the time-delays of cross correlation to understand how information is transferred over time. We use MATLAB's built-in correlation functions, xcorr, for cross correlation.

Lastly, using MATLAB's built in 'meanfreq' function, we find the mean frequency distribution in the astrocyte networks (any unique imaging sequence) as shown in Fig 2F. As we are interested in using Fourier analysis to provide an average measure of activity for any given trace, we apply another smoothing operation (MATLAB's smoothdata function) on the traces solely for Fourier analysis. We argue this smoothing provides us with a more faithful mesoscopic quantity for the frequency of a trace (see section on Information theory for handling the 'minor' fluctuations that occur in astrocyte traces). From the cross correlation, we can extract time delays associated with peak cross correlation between any pair of traces as shown in Fig 2I. We use these time delays to infer information speed in our networks, as we know the distance between any two object centers from FogBank. Thus, from these metrics, we quantify the activity levels in an astrocyte population, and we can robustly assess information coupling, speed, and activity within any astrocyte network.

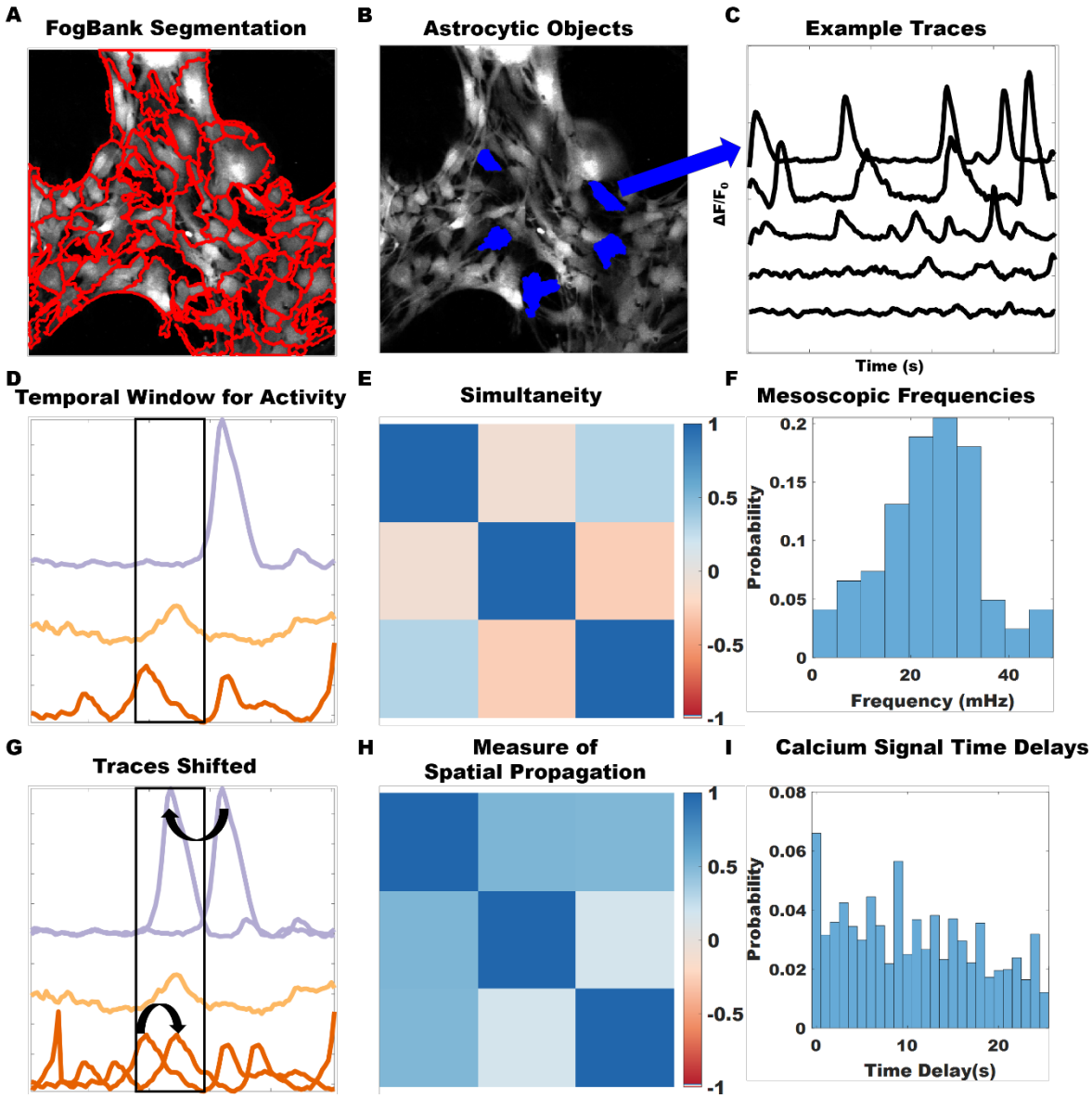

Fig 2: Dense astrocyte networks segmented and DFF traces extracted in order to uncover collective coupling within networks. (A) Example FogBank mask. (B) Subset of astrocyte elements extracted. (C) DFF traces for the five objects previously shown. (D) Example traces. Box shown to demonstrate overlap for simultaneity. (E) Pearson correlation matrix for traces in (D). (F) Mean, mesoscopic frequencies for all objects shown in (A). (G) Same traces as in (D) but with the bottom one shifted to demonstrate the time-delay overlap with the other traces. (H) Cross correlation matrix for time-shifted traces. (I) From cross correlation matrices, we can find the distributions of time delays associated with peak correlation. These time delays may be 0 which indicates simultaneity in astrocyte activity.

Information Theoretic Approach to Astrocyte Networks

Correlations allow us to understand the global characteristics of an ensemble of active nodes (in this case, astrocytes). However, we can alternatively view the dynamics in our astrocyte networks as a dynamical system that is affected by individual astrocytes, i.e., the local dynamics of one trace affecting the global dynamics observed. This approach has been well documented experimentally (e.g. with neuronal MRI data) and theoretically[35–43] . A limitation of correlations is that the global characteristics of a network are studied by assessing each cell's

connections to others in the network. Information theory helps overcomes such limitation. With an information theoretic approach, a network can be analyzed for each individual astrocyte, providing a measure of the mean field for collective dynamics. Furthermore, this approach provides a robust metric for assessing each individual astrocyte's contribution to the mean field.

To implement this approach, from the traces extracted, we then convert the traces into states using symbolization[35,44]. This symbolization enables interpretable data; we take the time traces shown in Fig 3A, amplitude order each timepoint in a window and convert this set of timepoints into a state (an example suite of states is available in Fig 3B), and then convert the traces into symbol sequences visualized in Fig 3C. From this symbol sequence, we can find the probability distributions of states (Fig 3D), from which in turn we can compute the information entropy for these calcium traces. Amplitude ordering entails choosing two parameters, m and l, where m defines the embedding dimension[35,43] (the symbol set size that functions as a coarse-graining window) and l denotes the time delay[43]. A more comprehensive review of this symbolization method can be found in Refs[35–37,39,41–44]. Based on our experimental observation of the duration of calcium events in our data, we chose m=5 and l=1. We choose m to smooth out noise without losing actual spikes in the data. Because m takes the role of the coarse-graining window, l ca be kept at its minimum (l=1) to prevent further information downsampling. We validated this analysis on both regular and chaotic time series data.[37]

Additionally, we analyze the information content of astrocyte networks with partitioned entropy. Partitioned entropy $h_a(\tau)$ is a useful metric for understanding the time-evolution of states over a certain window[37]:

$$h_a(\tau) = -\sum_{i=1}^{m!} p_{ai}(\tau) \ln\left(p_{ai}(\tau)\right) \quad \text{(Eq 1)}$$

where $p_{ai}(\tau)$ represents the probability that the system evolves from state a to state i at τ timesteps. Partitioned entropy differs from canonical entropy as it is a function of time. A schematic for understanding partitioned entropy is shown in Fig 3E.

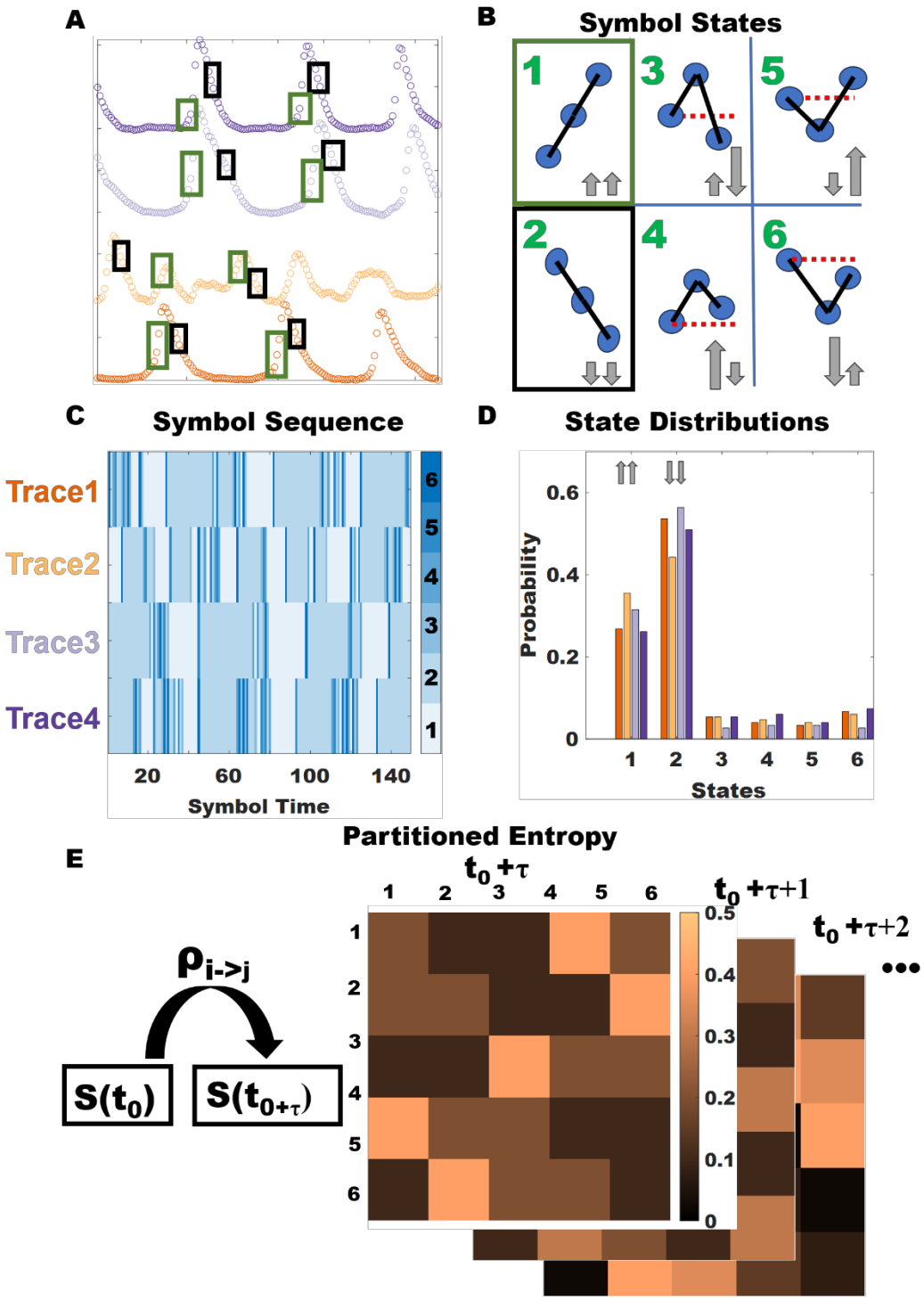

Fig. 3: Methods for Information Theoretic Approach to Collective Astrocyte Dynamics. (A) Astrocyte traces. Boxes correspond to example symbol states. (B) Symbol states. In this figure, have used an m of 3 as this corresponds to 6 possible states for every time window (m!=6). We note, using grey arrows, the physical dynamics behind each state (for states 1 and 2, the same size for the arrows is for visual purposes). (C) Symbol sequences for the traces shown previously. (D) Probability distributions of the six states shown in the symbol sequences. (E) Example subset of transition probabilities from states to future states for some given tau for any particular state 'i'. See Equation 1 for more details.

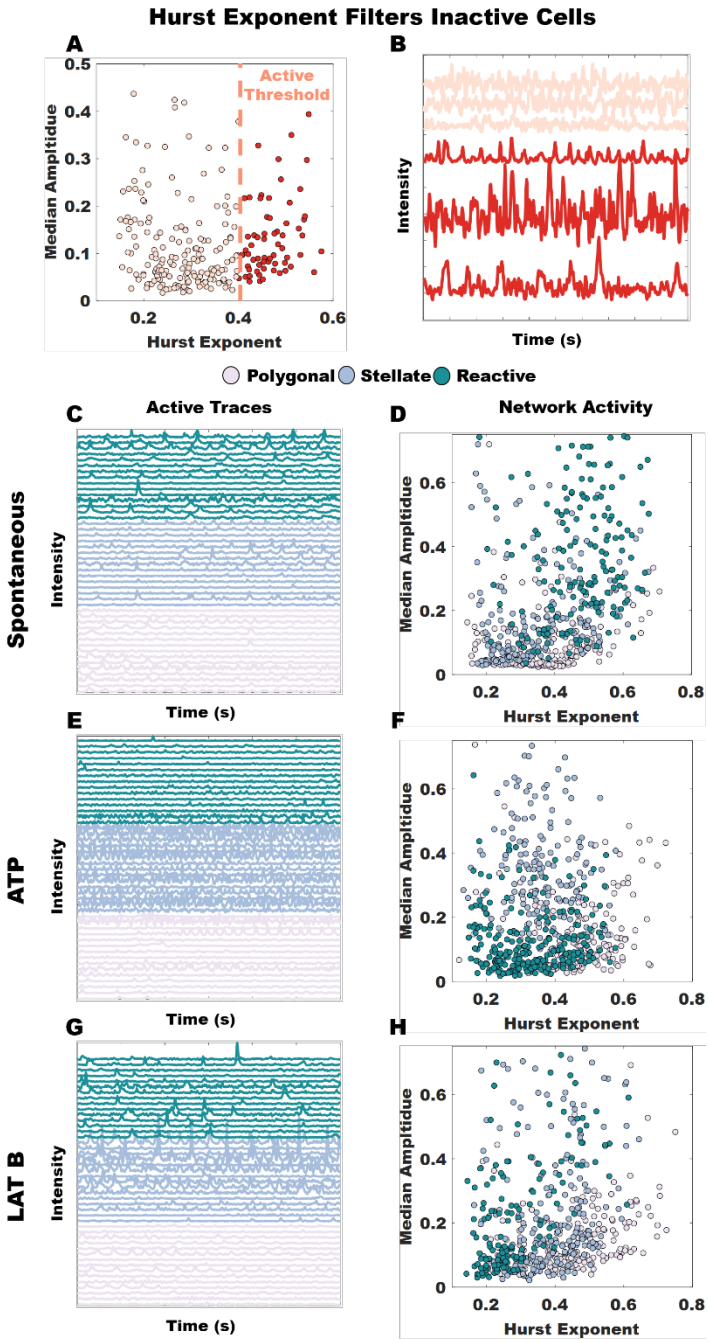

Fig 4: Activity of differing astrocytes. We measure activity by filtering out traces without persistent behavior using the Hurst exponent. (A) We filter astrocyte traces by thresholding their Hurst exponent at .4. (B) Example traces of active cells (red, darker shade—traces with Hurst exponent values higher than .4) and inactive cells (light pink, lighter shade). (C) Examples of active traces in spontaneous imaging sets. (D) Plotting active cell percentage versus median amplitude of ΔF/F traces. We find polygonal traces to be the least active. (E) Active traces for ATP stimulated cells. (F) ATP stimulates higher activity for polygonal and stellate astrocytes relative to spontaneous activity. (G) Active traces of LATB stimulated cells. (H) We notice the largest separation across activity patterns for LATB.

Next we perturbed the cell environment using ATP and Latrunculin B in order to understand how the environment impacts collective astrocyte signaling. For all results in which a p-value is specified, we use a one-way ANOVA test. We set $\alpha=0.05$ for our comparison tests.

Assessment of Astrocyte Activity

We assess astrocyte activity by comparing the median amplitude values of $\Delta F/F_0$ (DFF) traces and active cell percentages (the number of cells with DFF traces that pass through the Hurst filter) in the given networks. Each datapoint is found by taking the median of the top 75% (roughly corresponds to firing activity) of amplitude values per trace for all traces in a well and represents $O(10^2)$ cells. Our analysis only includes cells considered to be 'active;', as shown in Figs. 4C,E, F.

We find that polygonal astrocytes are the least active under spontaneous conditions. Fig 4C demonstrates the small amplitudes of active polygonal astrocytes relative to stellate and reactive cells, as shown in Fig 4D. We notice that reactive cells have the highest Hurst exponent and firing amplitudes of all networks. We comment that the activity patterns for stellate astrocytes includes FogBank objects that may contain more 'dead' area due to the presence of processes while reactive cells are more bloated and better represented by a FogBank mask. These global characteristics displayed by comparing median amplitudes and active percentages confirm previous literature regarding the relatively quiescent nature of polygonal astrocyte networks[15].

ATP increases the activity in polygonal and stellate networks. We notice, in Fig 4E, that ATP decreases the activity in reactive networks compared to polygonal and stellate ones. The differences in this effect on the traces translates well when we compare median amplitudes and Hurst exponents in Fig 4F. Stellate assumes a markedly stronger affinity to ATP than polygonal and reactive astrocytes. Interestingly, reactive astrocytes are tightly clustered for lower values while stellate astrocytes assume more heterogeneity in their activity distribution, as observed in Fig 4F. Moreover, we notice that ATP induces strong calcium dynamics in polygonal astrocytes. While introduction of ATP generating more calcium dynamics may seem obvious, this effect is significant as polygonal astrocytes tend to have comparable median amplitudes to reactive astrocytes, which previously we saw as the most active phenotype under control conditions.

We find that for all phenotypes LATB causes an increase in active behavior with the exception of reactive networks. These results suggest that perturbations do not affect reactive networks in the same manner as polygonal and stellate ones. Activity does not completely vanish (notice some strong peaks in Fig 4G), however we observe a even tighter cluster for very low values for reactive networks under LATB in comparison to an already reduced cluster for reactive networks influenced by ATP. We discover, for both polygonal and stellate astrocytes, that LATB increases overall calcium signaling. These results (Fig 4H) indicate that for stellate and polygonal networks, LATB can be said to have a comparable effect of driving increased network activity. Overall, it is concluded that these activity metrics distinguish networks based upon physiological state and environment; these networks respond uniquely relative to each other.

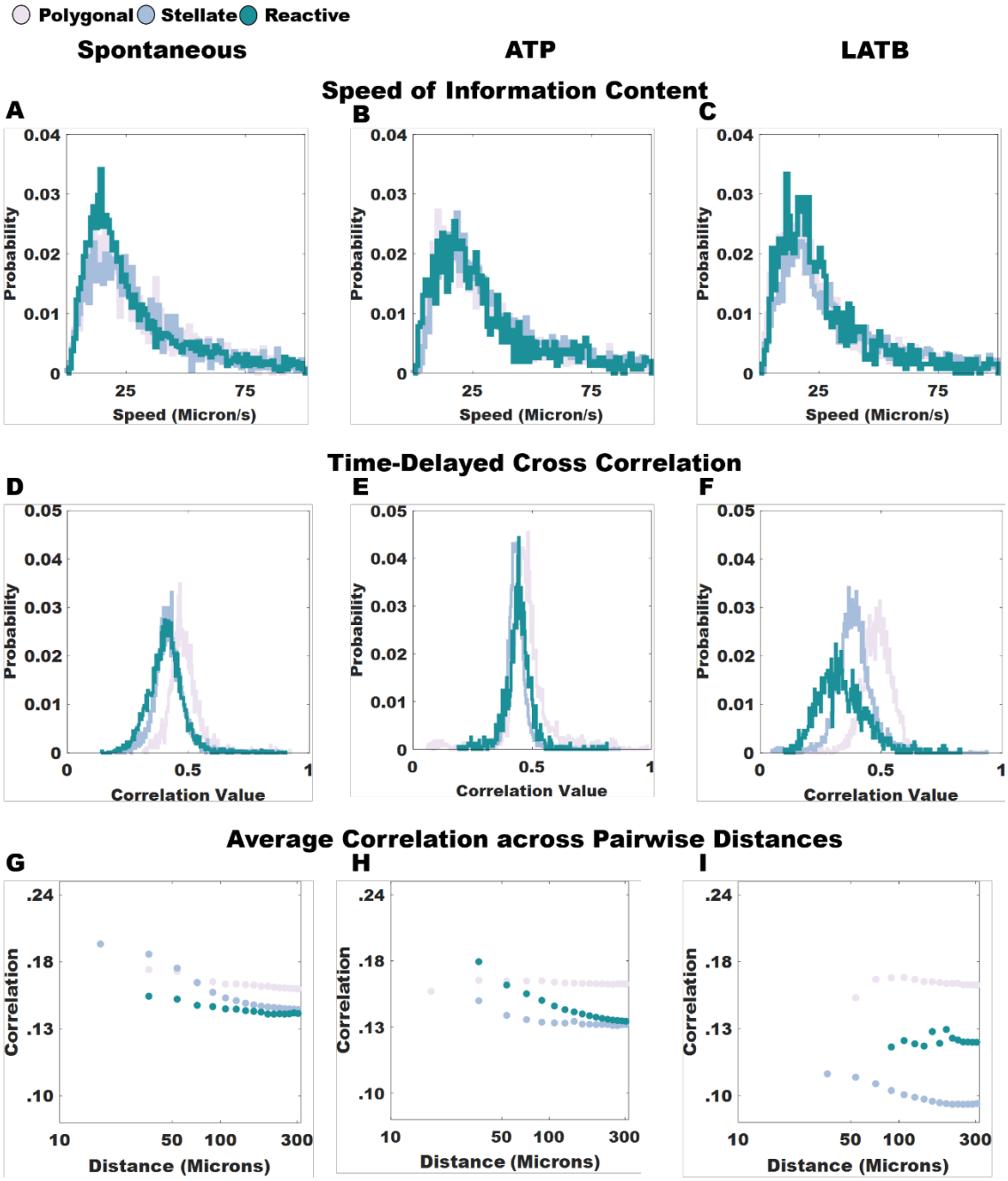

Fig 5: Speed and correlation analysis of morphologically distinct astrocytes. Speed of information transfers are shown in (A) for spontaneous wells, (B) for ATP-stimulated wells, and (C) for LATB-stimulated wells. Information speed is dependent upon neither morphology nor condition of the well. (D) Cross correlation of spontaneous astrocytes. (E) Cross correlation of ATP astrocytes. (F) Cross correlation of LATB astrocytes. (G) Reactive and stellate astrocytes display more local behavior. (H) Mean cross correlation vs distance for ATP astrocytes. (I) Mean cross correlation vs distance for LATB astrocytes. We notice the more prominent separation in curves.

Spatial and temporal relationships of signaling among active astrocytes

An important metric for understanding information flow is information speed. We do not track calcium flow, but can track the information as a function of time and distance between cells. Although we notice differences in the activity rates of astrocytes, we note that the speed of

information transfer does not vary significantly across any perturbation or morphology within the range of 20 μm/s to 30 μm/s. Moreover, the distributions in Figs 5A-C are comparable in terms of distribution shape; this shape remains consistently fat-tailed even under perturbation from ATP (Fig 5B) and LATB (Fig 5C). The median speeds of information content for spontaneously active polygonal, stellate, and reactive astrocytes are 27 μm/s, 29 μm/s, and 23 μm/s, respectively. Comparing the phenotypes under spontaneous conditions, the median speeds are significantly different when for polygonal versus reactive (p=1.1e-4) and for stellate versus reactive (p=1.7e-5). The median speeds of polygonal and stellate networks are not significantly different (p=0.98). The median speeds of information content for ATP-stimulated polygonal, stellate, and reactive astrocytes are 28 μm/s, 30 μm/s, and 27 μm/s, respectively. When perturbed by ATP, the median speeds are not significantly different across phenotypes (polygonal versus stellate p = 0.98, polygonal versus reactive p = 0.67, and stellate versus reactive p=0.71). The median speeds of information content for LATB-stimulated polygonal, stellate, and reactive astrocytes are 22 μm/s, 30 μm/s, and 23 μm/s, respectively. During perturbation with LATB, the median speeds are significantly different when comparing polygonal to stellate (*p≈0)* and when comparing stellate to reactive (*p≈0)*. Polygonal and reactive are not significantly different (*p≈1*).

To provide understanding of the spatial relationships in astrocyte communication, we quantify cross correlation distributions in active astrocytes. The median cross correlation values for spontaneously active polygonal, stellate, and reactive astrocytes are 0.47, 0.42, and 0.41, respectively (Fig. 5D). Polygonal astrocytes are more correlated than stellate and reactive astrocytes. For spontaneously active astrocytes, there exists a difference for all the morphologies (polygonal versus stellate *p≈0*, polygonal versus reactive *p≈0*, and stellate versus reactive *p=3.5e-9).* However, we note the larger separation between polygonal correlations and both stellate and reactive correlations than the separation between stellate and reactive network correlations. The median cross correlation values for ATP-stimulated polygonal, stellate, and reactive astrocytes are 0.47, 0.43, and 0.44, respectively (Fig. 5E). Similarly to spontaneously active networks, astrocyte networks induced with ATP retain significantly different cross correlation characteristics (polygonal versus stellate *p≈0*, polygonal versus reactive *p≈0*, and stellate versus reactive *p*=8.6e-5). We observe similar separations between the distributions as compared to spontaneous correlation distributions between the morphologies. The median cross correlation values for LATB-stimulated polygonal, stellate, and reactive astrocytes are 0.48, 0.38, and 0.33, respectively (Fig. 5F). When introducing LATB into an active astrocyte network, we continue to find statistically significant differences across phenotypes and additionally find the largest separation in any correlation distribution as visualized in Fig. 5L (For LATB, polygonal to stellate *p≈0*, polygonal to reactive *p≈0*, and stellate to reactive *p≈0*). Polygonal astrocytes display higher cross correlation values under spontaneous conditions (Fig. 5D) and under the influence of ATP (Fig. 5E). Additionally, we were surprised by the results under LATB-perturbed conditions (Fig. 5F). Notice the distinct separation of distributions between reactive, stellate, and polygonal astrocytes. Recall that LATB is a driver for encouraging network activity in astrocytes (Fig 4G-H). Moreover, it seems to disrupt the connections across time between astrocytes, suggesting that network functionality is dependent upon the initial morphology. The distinct separation, only seen under LATB perturbed conditions, suggests that indeed morphology plays a significant role in the communication patterns present in astrocyte cultures.

Next, we analyze cross-correlation versus distance. Interestingly, when we compare the cross correlation values across distance under spontaneous conditions, we see that polygonal astrocytes maintain the longest range of correlation while reactive and stellate cells display comparable local spatial behavior, with slight more locality for reactive astrocytes for distances below ~100 μm (Fig. 5G). The ATP-perturbed condition showcases comparable behavior to spontaneous (Fig. 5H). The LATB-perturbed condition shows that reactive and stellate astrocytes still behave more locally than polygonal astrocytes (Fig. 5I).

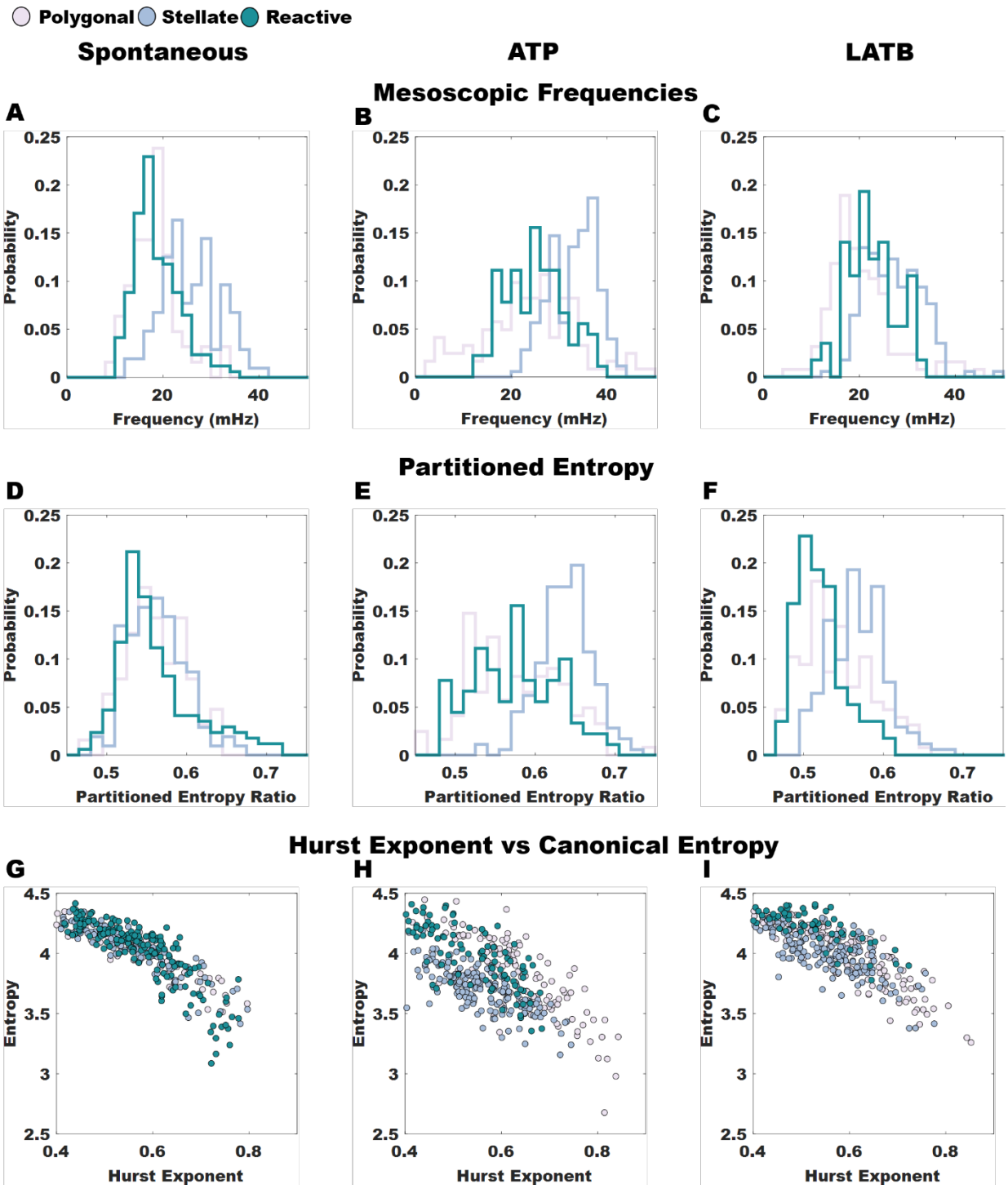

Fig 6: Mesoscopic and local dynamics. Frequency and entropy results for morphologically distinct astrocytes. (A) Fourier mean frequency distributions for spontaneous astrocytes. (B) ATP-stimulated frequencies. (C) LATB-stimulated frequencies. (D) Partitioned entropy ratio for spontaneous astrocytes. (E) Partitioned entropy ratios for ATP-stimulated astrocytes. (F) Partitioned entropy ratios for LATB-stimulated astrocytes. We note that these distributions allow for additional insight into the local dynamics of astrocytes. (G) System entropy, not partitioned, for all phenotypes in spontaneous wells versus their Hurst (autocorrelation) exponent. (H) System entropy versus Hurst for ATP astrocytes. (I) System entropy versus Hurst for LATB astrocyte networks.

Symbolization highlights temporally local dynamics

When analyzing the correlation values of active networks, we note that these values represent the global, mesoscopic properties of a network. In other words, correlation values provide an understanding of how astrocytes interact with each other. We can further investigate astrocyte networks by understanding their temporally local dynamics; we do this by analyzing the entropy within any individual trace (this value is independent of the activity of any neighboring or far-away astrocyte in any network). We analyze the partitioned entropy of our astrocyte networks. We analyze the partitioned entropy over the course of 50 symbol points (corresponds to roughly 50 s). We note that this partitioned entropy refers to the entropy of states rather than the system itself. As a result, although partitioned entropy is ~$1/H_{max}$ the partitioned entropy itself (the numerator of the ratio) need not scale linearly with H_{max}, i.e. the ratio need not be higher when trace entropy values are lower. Generally, partitioned entropy is a measure for characterizing limit-cycle (stable oscillatory) behavior in traces. Quantifying and defining whether astrocytes signal chaotically is outside the scope of this study.

To provide more intuition behind the information theoretic results, we contrast these analytics with the mean frequencies (a metric comparably derived for individual traces independently) within networks. Fourier frequencies here represent the average value taken from the power spectrum and describe a mesoscopic metric for understanding information in a network. The median frequency values for spontaneously active polygonal, stellate, and reactive astrocytes are 18 mHz, 25 mHz, and 18 mHz, respectively (Fig. 6A). For spontaneously active astrocytes, stellate astrocytes display more frequent events than polygonal and reactive astrocytes, which have more comparable frequency distributions (polygonal versus stellate $p=6.1e-19$, polygonal versus reactive $p=0.9027$, and stellate versus reactive $p\approx0$). The median frequency values for ATP-stimulated polygonal, stellate, and reactive astrocytes are 24 mHz, 34 mHz, and 25 mHz, respectively (Fig. 6B). The frequency distributions for ATP-stimulated astrocytes display a comparable statistical comparison as to the spontaneous active networks; polygonal and reactive networks do not display different distributions (p=0.39) while stellate frequencies are statistically different than both polygonal and reactive ones (polygonal versus stellate $p\approx0$, and stellate versus reactive $p=5.4e-18$). The median frequency values for LATB-stimulated polygonal, stellate, and reactive astrocytes are 19 mHz, 27 mHz, and 22 mHz, respectively (Fig. 6C). The same trend exhibited by the previous frequency distributions continues for LATB affected networks where we see stellate astrocytes differing significantly from polygonal (p=2.0e-19) and reactive (p=1.1e-4) astrocytes. Here, polygonal and reactive astrocytes still display statistically different frequency distributions but less so than in previous conditions (p=0.021).

We look at the partition entropy ratios for astrocytes in networks. The median entropy ratio values for spontaneously active polygonal, stellate, and reactive astrocytes are 0.56, 0.56, and 0.55, respectively (Fig. 6D). Surprisingly, the dynamical information contained within spontaneous active astrocytes, as measured by partitioned entropy, does not differ at all between any phenotype (polygonal versus stellate $p=0.998$, polygonal versus reactive $p\approx1$, and stellate versus reactive $p=0.997$). The median ratios for ATP-stimulated polygonal, stellate, and reactive astrocytes are 0.58, 0.64. and 0.57, respectively (Fig. 6E). Similar to the Fourier results for ATP, stellate astrocytes have a different information content than polygonal ($p\approx0$) and reactive ($p\approx0$). We cannot conclude any differences between polygonal and reactive partitioned entropy distributions ($p=0.85$). The median entropy ratios for LATB-stimulated polygonal,

stellate, and reactive astrocytes are 0.54, 0.57, and 0.52, respectively (Fig. 6F). LATB alters the entropy over time across all phenotypes (polygonal versus stellate *p=3.5e-8*, polygonal versus reactive *p*=1.5e-3, and stellate versus reactive *p=3.2e-15*). In sum, partitioned entropy enhances our understanding of the collective dynamics of these networks as the metric further highlights difference in the information contained in a network (for ATP and LATB perturbed networks) while revealing similar entropy as a function of time for spontaneous states of astrocytes.

System entropy (entropy with a qualifier to distinguish it from partitioned entropy) is the canonical measure for information. The Hurst exponent, as previously described, is a more rigorous metric for characterizing autocorrelation in a time series. Both of these quantities define and describe actual, temporally local dynamical behavior for any individual astrocyte in a network. Both metrics, however, do not consider the behavior of other astrocytes, and, thus, can both be used to assess mean field (collective) behavior of astrocytes in a network. When we compare system entropy as a function of the Hurst exponent, we conclude relevant takeaways. The first is that there exists a range of entropy for which a Hurst exponent may belong. This range is not exactly reciprocal for all results plotted as the range for Hurst exponents for any given entropy exhibits a larger width. Nonetheless, prominent features of this visualization are that despite the more pronounced activity of reactive astrocytes (Fig. 4B) and the higher mean frequency of stellate astrocytes (Fig. 6A), we find that when astrocytes spontaneously fire, they exhibit the same amount of information content (Fig. 6G). While k-means clustering does not find prominent clusters, we note that this effect is minimized by the presence of ATP (Fig. 6H). The narrow band in the spontaneous condition (Fig 6G) disappears, and we see more varied information content. Stellate astrocytes tend to have lower entropy than reactive astrocytes while polygonal astrocytes have a higher Hurst exponent. Lastly, while stellate astrocytes incubated in LATB have lower entropy relative to their peers, we see that the narrow band is recovered (Fig 6I), indicating a more similar propensity for transmitting information despite the different global characteristics previously described in our results.

Discussion

Collective astrocyte dynamics are rich in information. Using methods of cross-correlation, Hurst filtering, and symbolization, we discovered that collections of astrocytes behave differently when they are in distinct states, specifically maturing (polygonal), healthy (stellate), or injured (reactive). Our systematic analysis of the collective dynamics of slow Ca^{2+} activity within dense astrocyte networks provides insights into information capacity (correlations and canonical entropy, Figs. 5D-I and Figs. 6G-I) and information flow (information speeds and partitioned entropy, Figs. 5A-C and Figs 6D-F). We further characterize how astrocyte networks in these distinct states respond when the energy or biomechanics of the system is altered.

First, our measurements allow us to differentiate information capacity from cell activity. We find that polygonal astrocytes in control conditions, which are relatively quiescent,[15] carry the same amount of information when calcium waves are present as stellate and reactive astrocytes, the more naturally active astrocyte states. Thus, the difference in expression of the astrocyte markers AQP4 and Cx43, seen in stellate and reactive astrocytes, affect the percentage of active cells and their correlations, but not the information capacity of the network.

Our second main finding relates to the speed of information flow in the network, which we infer from time-delay cross correlations in dense astrocytes networks (Figs. 5A-C). We discovered that for all conditions investigated, the speed of information flow was approximately 10-30 μm/sec, consistent with the speed of Ca^{2+} waves measured directly in prior studies [24,45,46]. Our findings confirm that, for all morphologies studied, Ca^{2+} waves are the primary mechanism of cell-to-cell information exchange, limiting the speed of information flow among astrocytes. The speed of information flow is furthermore measured at a higher activity state of astrocytes (modulated by addition of ATP), and at lower actin polymerization conditions[22] (reduced via Latrunculin B). Neither perturbation significantly impacts the speed of information flow, indicating that Ca^{2+} dynamics is the dominant form of communication in astrocyte networks for all states and environmental conditions investigated.

Finally, our work provides insights into the flow of information as a function of distance between cells (Figs. 5G-I). The proteins that support cell-cell coupling, Cx43 and AQP4, are expressed at higher levels in stellate and reactive cells, and our results suggest this may be why stellate and reactive networks exhibit higher local correlations. These correlations decrease rapidly with distance, consistent with the role of astrocytes as "territorial cells"[6] with a local impact. Moreover, we find that this strong local correlation and coupling strongly depends on actin polymerization: Latrunculin-B significantly lowers correlations in both stellate and reactive astrocytes. Surprisingly, while the coupling is local in stellate and reactive cells, we find long distance coupling among active cells in polygonal networks.

Overall, our work shows that activity, information capacity, and information flow provide complementary insights into the collective action of astrocytes. Our study also provides a systematic baseline of three complementary astrocyte states and key perturbations that will support future studies of astrocyte network function in health and disease.

Acknowledgments

The authors thank the University of Maryland Imaging Incubator Core Facility for providing and maintaining the systems used in collecting images for this work. This work was supported by US Air Force Office of Scientific Research Astro-COLL grant FA9550-21-1-0352.

Software Availability

Software has been made available on GitHub at:
https://github.com/losertlab/Astrocyte_CollectiveNetworkInformation

1. Bellot-Saez, A., Kékesi, O., Morley, J. W. & Buskila, Y. Astrocytic modulation of neuronal excitability through K+ spatial buffering. *Neuroscience & Biobehavioral Reviews* **77**, 87–97 (2017).

2. Mahmoud, S., Gharagozloo, M., Simard, C. & Gris, D. Astrocytes Maintain Glutamate Homeostasis in the CNS by Controlling the Balance between Glutamate Uptake and Release. *Cells* **8**, 184 (2019).
3. Mola, M. G. *et al.* Cell Volume Regulation Mechanisms in Differentiated Astrocytes. *Cell Physiol Biochem* **55**, 196–212 (2021).
4. Bélanger, M., Allaman, I. & Magistretti, P. J. Brain Energy Metabolism: Focus on Astrocyte-Neuron Metabolic Cooperation. *Cell Metabolism* **14**, 724–738 (2011).
5. Araque, A., Parpura, V., Sanzgiri, R. P. & Haydon, P. G. Tripartite synapses: glia, the unacknowledged partner. *Trends in Neurosciences* **22**, 208–215 (1999).
6. Volterra, A. & Meldolesi, J. Astrocytes, from brain glue to communication elements: the revolution continues. *Nat Rev Neurosci* **6**, 626–640 (2005).
7. Dzyubenko, E., Prazuch, W., Pillath-Eilers, M., Polanska, J. & Hermann, D. M. Analysing Intercellular Communication in Astrocytic Networks Using “Astral”. *Frontiers in Cellular Neuroscience* **15**, (2021).
8. Abrego, L., Gordleeva, S., Kanakov, O., Krivonosov, M. & Zaikin, A. Estimating integrated information in bidirectional neuron-astrocyte communication. *Phys. Rev. E* **103**, 022410 (2021).
9. Perea, G., Sur, M. & Araque, A. Neuron-glia networks: integral gear of brain function. *Frontiers in Cellular Neuroscience* **8**, (2014).
10. Bazargani, N. & Attwell, D. Astrocyte calcium signaling: the third wave. *Nature Neuroscience* **19**, 182–189 (2016).
11. Araque, A. *et al.* Gliotransmitters Travel in Time and Space. *Neuron* **81**, 728–739 (2014).
12. Scemes, E. & Giaume, C. Astrocyte calcium waves: what they are and what they do. *Glia* **54**, 716–725 (2006).

13. Wang, Y. *et al.* Accurate quantification of astrocyte and neurotransmitter fluorescence dynamics for single-cell and population-level physiology. *Nat Neurosci* **22**, 1936–1944 (2019).
14. Lia, A. *et al.* Calcium Signals in Astrocyte Microdomains, a Decade of Great Advances. *Frontiers in Cellular Neuroscience* **15**, (2021).
15. Wolfes, A. C. *et al.* A novel method for culturing stellate astrocytes reveals spatially distinct Ca2+ signaling and vesicle recycling in astrocytic processes. *J Gen Physiol* **149**, 149–170 (2017).
16. Agarwal, A. *et al.* Transient Opening of the Mitochondrial Permeability Transition Pore Induces Microdomain Calcium Transients in Astrocyte Processes. *Neuron* **93**, 587-605.e7 (2017).
17. Lawal, O., Ulloa Severino, F. P. & Eroglu, C. The role of astrocyte structural plasticity in regulating neural circuit function and behavior. *Glia* **70**, 1467–1483 (2022).
18. Zhou, B., Zuo, Y.-X. & Jiang, R.-T. Astrocyte morphology: Diversity, plasticity, and role in neurological diseases. *CNS Neuroscience & Therapeutics* **25**, 665–673 (2019).
19. Rodnight, R. B. & Gottfried, C. Morphological plasticity of rodent astroglia. *Journal of Neurochemistry* **124**, 263–275 (2013).
20. Gradisnik, L. & Velnar, T. Astrocytes in the central nervous system and their functions in health and disease: A review. *World J Clin Cases* **11**, 3385–3394 (2023).
21. Liddelow, S. A. & Barres, B. A. Reactive Astrocytes: Production, Function, and Therapeutic Potential. *Immunity* **46**, 957–967 (2017).
22. O'Neill, K. M. *et al.* Decoding Natural Astrocyte Rhythms: Dynamic Actin Waves Result from Environmental Sensing by Primary Rodent Astrocytes. *Adv Biol (Weinh)* e2200269 (2023) doi:10.1002/adbi.202200269.
23. Yu, P., Wang, H., Katagiri, Y. & Geller, H. M. An In Vitro Model of Reactive Astrogliosis and Its Effect on Neuronal Growth. *Methods Mol Biol* **814**, 327–340 (2012).

24. Giaume, C. & Venance, L. Intercellular calcium signaling and gap junctional communication in astrocytes. *Glia* **24**, 50–64 (1998).
25. Chalfoun, J. *et al.* FogBank: a single cell segmentation across multiple cell lines and image modalities. *BMC Bioinformatics* **15**, 431 (2014).
26. Giovannucci, A. *et al.* CaImAn an open source tool for scalable calcium imaging data analysis. *eLife* **8**, e38173 (2019).
27. Bowen, Z., Winkowski, D. E., Seshadri, S., Plenz, D. & Kanold, P. O. Neuronal Avalanches in Input and Associative Layers of Auditory Cortex. *Frontiers in Systems Neuroscience* **13**, (2019).
28. Simonsen, I., Hansen, A. & Nes, O. M. Determination of the Hurst exponent by use of wavelet transforms. *Phys. Rev. E* **58**, 2779–2787 (1998).
29. Generalized Hurst exponent. https://www.mathworks.com/matlabcentral/fileexchange/30076-generalized-hurst-exponent (2023).
30. Averbeck, B. B., Latham, P. E. & Pouget, A. Neural correlations, population coding and computation. *Nat Rev Neurosci* **7**, 358–366 (2006).
31. Panzeri, S., Schultz, S. R., Treves, A. & Rolls, E. T. Correlations and the encoding of information in the nervous system. *Proc Biol Sci* **266**, 1001–1012 (1999).
32. Cohen, M. R. & Kohn, A. Measuring and interpreting neuronal correlations. *Nat Neurosci* **14**, 811–819 (2011).
33. Kohn, A., Coen-Cagli, R., Kanitscheider, I. & Pouget, A. Correlations and Neuronal Population Information. *Annual Review of Neuroscience* **39**, 237–256 (2016).
34. Aguado, F., Espinosa-Parrilla, J. F., Carmona, M. A. & Soriano, E. Neuronal Activity Regulates Correlated Network Properties of Spontaneous Calcium Transients in Astrocytes In Situ. *J Neurosci* **22**, 9430–9444 (2002).

35. Daw, C. S., Finney, C. E. A. & Tracy, E. R. A review of symbolic analysis of experimental data. *Review of Scientific Instruments* **74**, 915–930 (2003).
36. Cao, Y., Tung, W., Gao, J. B., Protopopescu, V. A. & Hively, L. M. Detecting dynamical changes in time series using the permutation entropy. *Phys. Rev. E* **70**, 046217 (2004).
37. Shiozawa, K., Uemura, T. & Tokuda, I. T. Detecting the dynamical instability of complex time series via partitioned entropy. *Phys. Rev. E* **107**, 014207 (2023).
38. Lungarella, M., Pitti, A. & Kuniyoshi, Y. Information transfer at multiple scales. *Phys. Rev. E* **76**, 056117 (2007).
39. Schreiber, T. Measuring Information Transfer. *Phys. Rev. Lett.* **85**, 461–464 (2000).
40. Lehnertz, K. Ordinal methods for a characterization of evolving functional brain networks. *Chaos: An Interdisciplinary Journal of Nonlinear Science* **33**, 022101 (2023).
41. Staniek, M. & Lehnertz, K. Symbolic Transfer Entropy. *Phys. Rev. Lett.* **100**, 158101 (2008).
42. Staniek, M. & Lehnertz, K. Symbolic transfer entropy: inferring directionality in biosignals. **54**, 323–328 (2009).
43. STANIEK, M. & LEHNERTZ, K. PARAMETER SELECTION FOR PERMUTATION ENTROPY MEASUREMENTS. *Int. J. Bifurcation Chaos* **17**, 3729–3733 (2007).
44. Bandt, C. & Pompe, B. Permutation Entropy: A Natural Complexity Measure for Time Series. *Phys. Rev. Lett.* **88**, 174102 (2002).
45. Glaum, S. R., Holzwarth, J. A. & Miller, R. J. Glutamate receptors activate Ca2+ mobilization and Ca2+ influx into astrocytes. *Proceedings of the National Academy of Sciences* **87**, 3454–3458 (1990).
46. Charles, A. C., Merrill, J. E., Dirksen, E. R. & Sandersont, M. J. Intercellular signaling in glial cells: Calcium waves and oscillations in response to mechanical stimulation and glutamate. *Neuron* **6**, 983–992 (1991).